Journal of Materials Chemistry A

High-throughput Screening of Mechanically Interlocked Catenane Metal Complexes for Enhanced Electrocatalytic Activity

Journal:	*Journal of Materials Chemistry A*
Manuscript ID	TA-ART-09-2024-006497.R1
Article Type:	Paper
Date Submitted by the Author:	02-Nov-2024
Complete List of Authors:	Tamtaji, Mohsen; Hong Kong Quantum AI Lab Ltd Goddard III, William; California Institute of Technology Chen, Guanhua; Hong Kong Quantum AI Lab Limited; The University of Hong Kong, Department of Chemistry

High-throughput Screening of Mechanically Interlocked Catenane Metal Complexes for Enhanced Electrocatalytic Activity

Mohsen Tamtaji[1], William A. Goddard III[2], GuanHua Chen[1,3]**

[1]Hong Kong Quantum AI Lab Limited, Pak Shek Kok, Hong Kong SAR, 999077, China

[2]Materials and Process Simulation Center (MSC), MC 139-74, California Institute of Technology, Pasadena CA, 91125, USA

[3]Department of Chemistry, The University of Hong Kong, Pokfulam Road, Hong Kong SAR, 999077, China

*Corresponding Authors, email: ghc@everest.hku.hk and wag@caltech.edu

Abstract

Metal complexes have been thoroughly studied for various electrochemical reactions. Mechanically interlocked molecular machines, however, have not been studied for electrochemistry. In this study, we apply the concept of mechanically interlocked Catenane metal complexes with a dynamic coordination environment around the metal center for hydrogen evolution reaction (HER), CO_2 reduction reaction (CO_2RR), oxygen evolution reaction (OER), and/or oxygen reduction reaction (ORR). We utilized density functional theory (DFT) to perform a systematic high-throughput screening on 3d transition metals supported by Catenane metal complexes denoted as $M(II)_{CN6}$ and $Co(I)_{CNx=4,5,6}$. We found that among all the 3d transition metals, only monovalent Co(I) is suitable as an application as a molecular machine. Target catalysts aimed at high electrochemical as well as thermodynamic stabilities besides low HER, CO_2RR, OER, and ORR overpotentials. DFT results show that HER takes place on neighboring nitrogen atoms of $Cu(II)_{CN6}$ with an overpotential of 0.27 V. In addition, CO_2RR, OER, and ORR take place on the metal active sites of $Ti(II)_{CN6}$, $Co(II)_{CN6}$, and $Cr(II)_{CN6}$, with overpotentials of 1.12, 0.81, and 0.36 V, respectively. This work brings fundamental understandings into the discovery of state-of-the-art electrocatalysts by introducing the idea of a dynamic coordination environment.

Keywords: Molecular Machine, ORR, OER, HER, CO_2RR

Introduction

Mechanically interlocked molecules such as Catenanes consist of interlocked macrocycles[1,2] usually with a metal center that is surrounded by the interlocked coordination ligands.[3–6] These interlocked macrocycles possess a high degree of motion freedom around the metal center that may be controlled using external stimuli such as light, pH, or applied potential depending on the structure of the Catenane, the size of macrocycles, and the metal center.[7,8] The Catenane metal complex is highly stable thermodynamically and electrochemically because of the mechanical chelation,[9] positioning it as a promising candidate toward sustainable and efficient catalytic processes. Recent advancements in the field of Catenane metal complexes have demonstrated their potential in various catalytic applications due to their unique structural properties and dynamic behavior. The dynamic motions around the metal center present the opportunity to tune the interlocked coordination ligands,[10–13] electrocatalytic activity, and selectivity of the metal center. These positive attributes involving various catalytic aspects create pathways for advancing mechanical interlocking as an innovative approach to designing transition metal electrocatalysts. Despite the difficulties in experimentally synthesizing Catenane metal complexes and their low reaction yields,[7] their long-standing applications have recently led to the use of Catenane-coordinated transition metal complexes in chemical reactions such as electrocatalysis, cross-coupling, and photocatalysis.[9,14–18] For example, a two-dimensional metal-organic layer with anchored Cu(I) Catenane complexes is experimentally synthesized for high-fidelity cross-coupling reactions.[15] Catenane ligands ensure that Cu(I) is well-defined within its coordination environment and is kinetically stable, avoiding the uncontrolled creation of oxidized copper active sites and ensuring exclusive C-O coupling of substrates. In another work, a mechanically interlocked Catenane Cu(I) complex for the oxygen reduction reaction (ORR) was studied theoretically with the DFT-calculated overpotential of 1.81 V_{RHE} and synthesized with the

experimental overpotential of 0.84 V_{RHE} at -1 mA/cm^2 current density.[9] This work indicates that the isolation by two macromolecular rings does not prevent the Cu (I) metal center from being electrochemically active and the high-coordinated Cu (I) metal center can act as a catalytic site for the ORR.

Metal complexes such as single atom catalysts or molecular metal complexes for energy storage and conversion applications are of vital importance for the electrochemical ORR, the oxygen evolution reaction (OER), the hydrogen evolution reaction (HER), and the CO_2 reduction reaction (CO_2RR).[19–27] CO_2RR as a room temperature energy conversion approach can reduce anthropogenic emissions of CO_2 while producing value-added products.[25,28] ORR, OER, and HER are the main components of rechargeable metal-air battery and fuel cell applications for energy storage applications[29,30,39,31–38] Recently, a substantial amount of effort has been invested in designing metal complexes for electrochemistry through high-throughput screening.[40] For example, an FeRu metal complex was explored theoretically followed experimental synthesis for bifunctional ORR and OER along with rechargeable zinc-air battery application.[29] However, the coordination environment of these metal complexes remains static (non-dynamic) so that achieving changes in the catalytic activity of these complexes necessitates modifications to the coordination environment during their synthesis process. In addition, the scaling relationship limit hinders the development of these metal complexes toward enhanced catalytic activities.[41] Therefore, to overcome the limitation on the non-dynamic environment around the metal active site and address the scaling relationship limits, we have used the Catenane metal complexes.

Catenane metal complexes offer a unique advantage in modifying the activity of metal centers through the motion of macromolecules that change the metals' coordination environment. This strategic design of Catenane metal complexes with a dynamic coordination environment requires

systematic and in-depth investigations on the ORR, OER, CO_2RR, and HER mechanisms along with the synthesizability and stability of these catalysts. As far as we know, no Catenane metal complex has yet been systematically examined for OER, ORR, HER, and CO_2RR. Can all the 3d transition metals serve as the metal center? What is the catalytic stability and activity of 3d transition metals towards ORR, OER, CO_2RR, and HER?

In this work, we use mechanically interlocked molecules for several electrochemical reactions through high-throughput computational screening. We investigate a series of metal complexes labeled containing 3d transition metals. We discover that the $Ti(II)_{CN6}$ is appropriate for CO_2RR, $Cu(II)_{CN6}$ is appropriate for HER, $Cr(II)_{CN6}$ is appropriate for ORR, and $Co(II)_{CN6}$ is appropriate for OER, mainly because of the weakening of scaling relationship limit. This provides an in-depth investigation of mechanically interlocked Catenanes for electrochemical reactions and beyond.

Materials and Methods

Density Functional Theory (DFT) Calculations Details

We used density functional theory (DFT) calculations in Vienna ab initio Simulation Package (VASP, version 6.1.0) code.[42,43] The spin-polarized DFT calculations was performed using Perdew-Burke-Ernzerhof (PBE) functional[23,44] . While PBE functional has its deficiency in calculating the adsorption energy of carbon-containing intermediates, it has been effectively employed to investigate CO_2RR and CORR mechanisms,[45] showing good agreement with experimental results found in the literature.[46] We used DFT-D3 correction with the Becke-Johnson damping function to apply van der Waals (London dispersion) interactions.[47] We used VASPsol code with the water dielectric constant (ε=78.4).

As depicted in **Figure 1a**, we constructed a single Catenane molecule with a metal single atom at the center. A box with the size of 27.96 Å×21.56 Å×21.56 Å was used along the x, y, and z

directions to minimize interactions between periodic images. A plane wave energy cutoff of 500 eV is utilized and the Brillouin zone is sampled by using the 1×1×1 Monkhorst-Pack k-point scheme. The force and energy convergence criteria were set to 0.02 eVÅ^{-1} and 10^{-5} eV, respectively, for the structural relaxations. In addition, the energy convergence criterion was set to 10^{-6} eV for the single-point energy calculations. The vibrational frequency and entropy calculations were conducted to consider the Zero-point, enthalpic, and entropic contributions of phonons at 298.15 K.[23]

Results and discussion

The mechanically interlocked M(I or II)$_{CNx=4,5,6}$ structure where M represents 3d transition metals and x stands for the number of neighboring nitrogen atoms around the metal center, can enhance electrochemical reactions. The side view of the M(I or II)$_{CNx=4,5,6}$ structure is depicted in **Figure 1a**, where M is Ti, V, Cr, Fe, Mn, Co, Cu, Ni, or Zn. Moreover, the structure of one macrocycle denoted as M(I or II)$_{CNx=2,3}$ is shown in **Figure S1**. The thermodynamic stability as well as electrochemical stability of these Catenane metal complexes were examined by calculating formation energy ($E_{formation}$) as well as dissociation potential (U_{diss}), respectively:[23]

$$E_{formation} = E_{M(I\text{ or }II)CN_{x=4,5,6}} - E_{CNx} - E_{M}^{bulk} \quad (1)$$

$$U_{diss} = U_{diss}^{o}(M - bulk) - \frac{E_{formation}}{Ne} \quad (2)$$

where $E_{M(I\text{ or }II)CN_{x=4,5,6}}$ and E_{CNx} are the total energy of M(I or II)$_{CNx=4,5,6}$ with and without the metal center, respectively. The metal atom's total energy in its most stable bulk form, the standard dissolution potential of the metal in its bulk structure, and the number of electrons that participated in the dissolution process are denoted as E_{M}^{bulk}, U_{diss}^{o}, and Ne, respectively (Supporting Information). **Figure S2** demonstrates the dissociation potential versus formation energy of M(I

or II)$_{CNx=2,3,4,5,6}$. All metal complexes are thermodynamically and electrochemically stable since they meet the $U_{diss}>0$ and $E_{formation}<0$ criteria. It is worth mentioning that, to further validate the stability of the Catenanes structure, other methods such as machine learning or kinetic simulations might be needed.[48,49] **Figure 1b** displays the dissolution potential and formation energy for M(I or II)$_{CNx=2,3,4,5,6}$ versus the number of nitrogen atoms neighboring the metal. CN6 metal complexes are more electrochemically and thermodynamically stable among all metal complexes because of their more positive dissociation potential and more negative formation energy, respectively.

Figure 1c shows the change in the energy of M(I or II)$_{CNx=4,5,6}$ with different numbers of nitrogen atoms. We see that except for monovalent Cu(I), all divalent metals, M(II), possess more negative energy for CN6 than for CN4 and CN5 by at least -0.5 eV. Therefore, we considered only the CN6 structure for all divalent metals for further catalytic calculations (M(II)$_{CN6}$). Interestingly, for the only monovalent 3d metal, Cu(I), the CN5 structure is the more stable configuration. In comparison, the CN4 and CN6 structures have energy levels that are 0.22 and 0.51 eV higher, respectively. Therefore, we conclude that the Cu(I) metal complex can go through the co-deformation by applying positive or negative voltages and act as the molecular machine. This is consistent with a very old publication explaining the alteration in the coordination environment of Cu(I) as a function of applied potential. Therefore, for monovalent Cu(I), we consider all CN4, CN5, and CN6 structures for further activity calculations (Cu(I)$_{CNx=4,5,6}$).

Figure 1d shows formation energies and dissociation potentials against the number of d orbital electrons. This volcano plot indicates the minimum formation energy at d electron number of 9 (highlighted by blue color) and the lowest dissolution potential at d electron number of 6 (highlighted by pink color). **Table S1** provides the values for the metals' dissolution potential, formation energy, and oxidation states. Cu(I)$_{CNx=4,5,6}$ and Cu(II)$_{CN6}$ possess less thermodynamic

stability because they possess less negative formation energies. Besides the formation energy of M(I or II)$_{CNx=4,5,6}$, the formation energy of metal-free CN4, CN5, and CN6 Catenane structures are calculated to be -7.00, -7.14, and -6.63 eV, respectively, with the two individual macrocycles as the reference, suggesting thermodynamic stability of the metal-free Catenane.

Following a comprehensive study on the electrochemical as well as thermodynamic stabilities of the Catenane metal complexes, we calculated the Gibbs free energies (ΔG) of reaction intermediates, including H, OOH, O, OH, OO, COO, COH, COOH, and CO, to evaluate their electrochemical activities. These Gibbs free energies are obtained as follows:

$$\Delta G_{int.} = E_{int.@M(I\text{ or }II)CN_{x=4,5,6}} - E_{M(I\text{ or }II)CN_{x=4,5,6}} - N_{CO_2}E_{CO_2} - N_{H_2}E_{H_2} + M_{H_2O}E_{H_2O} + \Delta E_{ZPE} - T\Delta S \quad (3)$$

where E_{CO_2}, E_{H_2O}, and E_{H_2} represent the energy of CO_2 (g), H_2O (g), and H_2 (g), respectively. N_{CO_2}, N_{H_2O}, and N_{H_2} represent the stoichiometric quantities of CO_2 (g), H_2O (g), and H_2 (g), respectively. $E_{M(I\text{ or }II)CN_{x=4,5,6}}$ and $E_{int.@M(I\text{ or }II)CN_{x=4,5,6}}$ are the total energy of M(I or II)$_{CNx=4,5,6}$ in the absence and presence of adsorbed intermediate (int.), respectively. ΔE_{ZPE} and TΔS are the zero-point energy (ZPE) and the entropy corrections, respectively, and T is the absolute temperature (=298.15 K), respectively.[50]

Figure 2a illustrates ΔG of H, OO, OOH, O, OH, COO, COOH, COH, and CO reaction intermediates for Cu(I)$_{CNx=4,5,6}$ and M(II)$_{CN6}$. **Figure S4** displays a histogram of Gibbs free energy variation with 130 data points. The average is 2.55 eV, the skewness is 0.20, and the standard deviation is 1.68 eV. **Figure 2b** displays a box plot of ΔG variation for each reaction intermediate, highlighting their standard deviation as well as average. The O, COH, and OH possess the largest standard deviations (1.47, 1.03, and 0.88 eV). In contrast, the more neutral intermediates such as

COO, CO, and OO possess the lower standard deviations (0.11, 0.11, and 0.19 eV) and smaller alteration in ΔG.

To examine the scaling relationship limit, a key issue in designing advanced CO_2RR, HER, ORR, and OER electrocatalysts, we conducted a linear regression for the ΔG of H, OO, OOH, O, OH, COO, COOH, COH, and CO intermediates. **Figure 2c-d** indicates that the scaling relationship among the intermediates is weak, matching a previous report.[51,52]. **Table S2** presents the R^2 values and linear relationship coefficients between the ΔG of H, OO, OOH, O, COO, COOH, COH, and CO intermediates and ΔG of OH intermediate. The R^2 values for the intermediates' dependency on ΔG_{OH} are below 0.84, indicating a weakened scaling relationship compared to single atom metal complexes, which have R^2 values close to 0.99 as previously reported.[23,53] This allows for independent adjustment of the Gibbs free energy of a specific intermediate.[54] However, this weakened scaling relationship doesn't allow us to achieve a universal descriptor to define the electrocatalytic activity of our metal complexes. Consequently, due to the weakened scaling relationship, designing mechanically interlocked metal complexes could be an effective strategy to overcome this limitation, potentially leading to highly active and selective electrocatalysts.

According to the Gibbs free energy values, we calculated the overpotentials for CO_2RR, HER, ORR, and OER. **Figure 3a** shows the high-throughput screening and **Figure 3b** shows a volcano plot of DFT-calculated CO_2RR, HER, ORR, and OER overpotentials against the number of d orbital electrons. **Figure S5** shows the DFT-predicted CO_2RR, HER, ORR, and OER overpotentials versus ΔG_{OH}. This shows that $Ti(II)_{CN6}$, $Cu(II)_{CN6}$, $Cr(II)_{CN6}$, and $Co(II)_{CN6}$ possess less overpotential for CO_2RR, HER, ORR, and OER, respectively.

Hydrogen Evolution Reaction (HER)

We investigated the HER on $M(II)_{CN6}$ and $Cu(I)_{CNx=4,5,6}$ through the following fundamental step:[54]

$$* + 0.5H_2 \rightleftharpoons H^* + e^- \quad (4)$$

Too strong hydrogen binding deactivates and poisons the metal sites, and too weak hydrogen binding prevents H atoms from attaching to the metal sites, hindering their ability to perform HER.[55] Thus, a catalyst with a ΔG_H closer to 0 would exhibit high activity for HER. **Figure 4a** displays HER profiles for metal complexes, indicating that HER on $Cu(II)_{CN6}$ leads to an overpotential of $\eta^{HER} = |\Delta G_H|/e = 0.27\ V_{RHE}$. **Figure 4b** displays the side view of H intermediate on the neighboring nitrogen site of $Cu(II)_{CN6}$ indicating that HER takes place on the neighboring nitrogen atoms rather than on the metal site.

CO_2 reduction Reaction (CO_2RR) towards CO production

We investigated the 2-electron transfer towards CO formation for CO_2RR at room temperature on $M(II)_{CN6}$ and $Cu(I)_{CNx=4,5,6}$ through the following fundamental steps:[56]

$$* + CO_2 \rightleftharpoons CO_2^* \text{ (adsorption)} \quad (5)$$

$$CO_2^* + 0.5H_2 \rightleftharpoons COOH^* + e^- \quad (6)$$

$$COOH^* + 0.5H_2 \rightleftharpoons CO^* + H_2O + e^- \quad (7)$$

$$CO^* \rightleftharpoons * + CO \text{ (desorption)} \quad (8)$$

$$CO^* + 0.5H_2 \rightleftharpoons COH^* + e^- \quad (9)$$

Before investigating the CO_2RR mechanism in-depth, the competitive HER should be studied. Too strong hydrogen binding deactivates and poisons the metal sites, hindering their ability to perform CO_2RR. Thus, a catalyst that weakly binds H but strongly adsorbs CO_2 might achieve high CO_2RR selectivity. The adsorption energy of H intermediate would show stronger over the neighboring nitrogen atoms (**Figure S7**), while CO_2RR intermediates tend to be more stable over the metal active site for all the metal complexes. **Figure 5a** displays ΔG_{CO2} against ΔG_H, indicating that CO_2 binds more strongly to the metal centers than H does to the neighboring nitrogen atoms, except for

$Cu(II)_{CN6}$ and $Co(II)_{CN6}$. Therefore, all metal complexes except for $Cu(II)_{CN6}$ and $Co(II)_{CN6}$, show selective HER over CO_2RR. Among these catalysts, $Ti(II)_{CN6}$ leads to the minimum CO_2RR overpotential.

Figure 5b displays the CO_2RR pathway for the $Ti(II)_{CN6}$. The green color indicates the potential-determining step (PDS), which represents the step that has undergone the maximum free energy change in the course of the electrochemical process. This shows that $Ti(II)_{CN6}$ possesses a low overpotential of $(\Delta G_{COOH} - \Delta G_{*+CO_2})/e = 1.12$ V with the $* + CO_2 \xrightarrow{H^+ + e^-} COOH^*$ step as PDS towards CO production. The inset displays the side view of 0.27 e^- Bader charge transfer from $Ti(II)_{CN6}$ to COOH with the Isosurface value of 0.005 e/Å^3. Blue color shows the region of charge deficiency and yellow color shows the region of charge availability. $Ti(II)_{CN6}$ possesses preferable CO_2RR selectivity to HER selectivity, with exothermic CO desorption and low CO_2RR overpotential. It is important to note that other reaction pathways toward C1 reaction products[57] are not possible. According to **Figure 5b**, the release of CO is spontaneous and exothermic,[58,59] while the hydrogenation of the CO intermediate is not favorable to produce a COH intermediate towards C1 products. **Figure 5c-d** shows the partial density of states (PDOS) of $3d_{x2-y2}$, $3d_{z2}$, $3d_{xz}$, $3d_{xy}$, and $3d_{yz}$ orbitals of Ti active site in $Ti(II)_{CN6}$ in the absence and presence of COOH. **Figure S8** shows the p_y, p_z, and p_x orbitals of the O atom in COOH intermediate adsorbed on $Ti(II)_{CN6}$. Therefore, the 3d orbitals of the Ti active site form a bonding orbital (σ) at $E-E_f$=-1.9 eV with the p_y, p_z, and p_x orbitals of the O atom in the COOH intermediate and an anti-bonding orbital at $E-E_f$=3.24 eV with the p_y and p_z orbitals of the O atom in the COOH intermediate.

Oxygen Evolution and Reduction Reactions (OER and ORR)

We studied the OER and ORR mechanisms by examining the backward and forward directions of the following electrochemical steps:[54]

$$* + O_2 \rightleftharpoons O_2^* \text{ (adsorption)} \quad (10)$$

$$O_2^* + 0.5H_2 \rightleftharpoons OOH^* + e^- \quad (11)$$

$$OOH^* + 0.5H_2 \rightleftharpoons O^* + e^- \quad (12)$$

$$O^* + 0.5H_2 \rightleftharpoons OH^* + e^- \quad (13)$$

$$OH^* + 0.5H_2 \rightleftharpoons * + H_2O + e^- \quad (14)$$

Similar to CO_2RR, the OER and ORR prefer to occur on the metal active site. **Figure 6a** displays the ORR pathway for $Cr(II)_{CN6}$ with an ORR overpotential of 0.36 V_{RHE}. This is comparable to the DFT-calculated ORR overpotentials of 1.81, 0.56, 0.38, 0.44, 0.43, 0.33, and 0.34 V for Cu(I)-Catenane[9], FeN4-SAC[23], FeFeN6-DAC[54], FeCoNiRu-HESAC[23], the benchmark Pt (111)[60], CoRu@N8V4[61], and CoCuN6-gra(OH)[62].

Figure 6a shows that the protonation of OH to produce and release H_2O is the rate-determining step (RDS). **Figure 6b** displays the side view of 0.42 e^- Bader charge transfer from $Cr(II)_{CN6}$ to the OH with the Isosurface value of 0.005 e/Å^3. Blue color shows the region of charge deficiency and yellow color shows the region of charge availability. **Figure 6c-d** shows the PDOS of $3d_{x2-y2}$, $3d_{z2}$, $3d_{xz}$, $3d_{xy}$, and $3d_{yz}$ orbitals of the Cr active site in $Cr(II)_{CN6}$ in the presence and absence of OH. The 3d orbitals of the Cr active site form a bonding orbital (σ) at $E-E_f$=-3.9 eV and an anti-bonding orbital at $E-E_f$=3.9 eV with the p orbital of the O atom in OH intermediate.

Figure 7a displays the OER pathway for $Co(II)_{CN6}$ with an OER overpotential of 0.81 V_{RHE}, comparable with DFT-calculated OER overpotential of 1.76 V_{RHE} for Cu(I)-Catenane.[9] **Figure 7a** indicates that the deprotonation of H_2O to produce OH intermediate is the OER rate-determining step (RDS). **Figure 7b** shows the side view of 0.45 e^- Bader charge transfer from $Co(II)_{CN6}$ to the OH intermediate with the Isosurface value of 0.005 e/Å^3. Blue color shows the region of charge

deficiency and yellow color shows the region of charge availability. **Figure 7c-d** shows the PDOS of $3d_{x2-y2}$, $3d_{z2}$, $3d_{xz}$, $3d_{xy}$, and $3d_{yz}$ orbitals of the Co active site in $Co(II)_{CN6}$ in the presence of OH intermediate. The 3d orbitals of the Co active site form a bonding orbital (σ) at $E-E_f$=-4.2 eV and anti-bonding orbitals at $E-E_f$=0.8 eV and $E-E_f$=1.0 eV with the p orbital of the O atom in OH intermediate.

Conclusion

This work introduces deep insights into the discovery of mechanically interlocked molecular machines such as dimeric, trimeric, and multimeric Catenanes by applying the concept of a dynamic coordination environment for electrochemistry at room temperature. Metal complexes are extensively reported for electrochemical reactions. Mechanically interlocked molecular machines, however, have not been systematically studied for electrochemistry using high-throughput screening. Thus, we use mechanically interlocked Catenane metal complexes with a dynamic coordination environment for hydrogen evolution reaction (HER), CO_2 reduction reaction (CO_2RR), oxygen evolution reaction (OER), and/or oxygen reduction reaction (ORR). Applying density functional theory (DFT), the thermodynamic and electrochemical stabilities of Catenane metal complexes denoted as $M(II)_{CN6}$ and $Co(I)_{CNx=4,5,6}$ are studied. Meanwhile, HER on the neighbor nitrogen atoms of $Cu(II)_{CN6}$ proceeds at overpotentials as low as 0.27 V. The CO_2RR, ORR, and OER occur on the metal active sites of $Ti(II)_{CN6}$, $Cr(II)_{CN6}$, and $Co(II)_{CN6}$, at the overpotentials of 1.12, 0.36, and 0.37 V. In summary, the comprehensive DFT calculations presented in this work pave the way for further experimental efforts by the community, despite challenges and difficulties in achieving high yields when synthesizing these mechanically interlocked metal complexes.

Associated Content

Supporting Information

Formation energies, scaling relationships, overpotentials, and additional figures as mentioned in the text (Word).

POSCAR and CONTCAR files of all the relaxed structures obtained in this work (zip file).

Conflicts of interest

The authors respectfully declare that there are no conflicts of interest to acknowledge for this research.

Data availability

Data will be available on request.

Acknowledgments

WAG thanks the US National Science Foundation (CBET-2311117) for support. GHC acknowledges financial supports by the General Research Fund (Grant No. 17309620) and Research Grants Council (RGC: T23-713/22-R). WAG and GHC acknowledge support from the Hong Kong Quantum AI Lab, AIR@InnoHK of the Hong Kong Government.

References

1 N. Pairault, F. Rizzi, D. Lozano, E. M. G. Jamieson, G. J. Tizzard and S. M. Goldup, *Nat. Chem.*, 2023, **15**, 781–786.

2 Y. Wang, Y. Zhang, Z. Zhou, R. T. Vanderlinden, B. Li, B. Song, X. Li, L. Cui, J. Li, X. Jia, J. Fang, C. Li and P. J. Stang, *Nat. Commun.*, 2020, **11**, 2727.

3 D. A. Leigh, R. G. Pritchard and A. J. Stephens, *Nat. Chem.*, 2014, **6**, 978–982.

4 S. M. Goldup, D. A. Leigh, T. Long, P. R. McGonigal, M. D. Symes and J. Wu, *J. Am. Chem. Soc.*, 2009, **131**, 15924–15929.

5 T. Ma, Y. Zhou, C. S. Diercks, J. Kwon, F. Gándara, H. Lyu, N. Hanikel, P. Pena-Sánchez, Y. Liu, N. J. Diercks, R. O. Ritchie, D. M. Proserpio, O. Terasaki and O. M. Yaghi, *Nat. Synth.*, 2023, **2**, 286–295.

6 J. Liu, M. Wu, L. Wu, Y. Liang, Z. Tang, L. Jiang, L. Bian, K. Liang, X. Zheng and Z. Liu, *Angew. Chemie*, 2023, **135**, e202314481.

7 D. J. Cárdenas, A. Livoreil and J. P. Sauvage, *J. Am. Chem. Soc.*, 1996, **118**, 11980–11981.

8 V. G. Sree, S. Naik, A. Jana, A. Kadam, S. Sekar, H. Im, H.-S. Kim, J. I. Sohn and C. Bathula, *J. Colloid Interface Sci.*, 2023, **633**, 589–597.

9 X. Mo, Y. Deng, S. K. M. Lai, X. Gao, H. L. Yu, K. H. Low, Z. Guo, H. L. Wu, H. Y. Au-Yeung and E. C. M. Tse, *J. Am. Chem. Soc.*, 2023, **145**, 6087–6099.

10 Y. Yao, Y. C. Tse, S. K. M. Lai, Y. Shi, K. H. Low and H. Y. Au-Yeung, *Nat. Commun.*, 2024, **15**, 1952.

11 G. Gil-Ramírez, D. A. Leigh and A. J. Stephens, *Angew. Chemie - Int. Ed.*, 2015, **54**, 6110–6150.

12 A. Bhadani and M. Kathiresan, *Org. Chem. Front.*, 2024, **11**, 2954–2980.

13 L. Zhang, Y. Qiu, W. G. Liu, H. Chen, D. Shen, B. Song, K. Cai, H. Wu, Y. Jiao, Y. Feng, J. S. W. Seale, C. Pezzato, J. Tian, Y. Tan, X. Y. Chen, Q. H. Guo, C. L. Stern, D. Philp,

R. D. Astumian, W. A. Goddard and J. F. Stoddart, *Nature*, 2023, **613**, 280–286.

14 L. Zhu, J. Li, J. Yang and H. Y. Au-Yeung, *Chem. Sci.*, 2020, **11**, 13008–13014.

15 Y. Shi, L. Zhu, Y. Deng, X. Mo, Y. Wang and E. C. M. Tse, *ChemRxiv*, , DOI:10.26434/chemrxiv-2024-hk44r.

16 Y. Deng, Z. Lu, S. K. Lai, X. Mo, S. He and D. Lee, *ChemRxiv*, , DOI:10.26434/chemrxiv-2024-tdjrk.

17 M. P. Tang, L. Zhu, Y. Deng, Y. X. Shi, S. Kin-Man Lai, X. Mo, X. Y. Pang, C. Liu, W. Jiang, E. C. M. Tse and H. Y. Au-Yeung, *Angew. Chemie - Int. Ed.*, 2024, **136**, e202405971.

18 Y. Jiao, L. Đorđević, H. Mao, R. M. Young, T. Jaynes, H. Chen, Y. Qiu, K. Cai, L. Zhang, X. Y. Chen, Y. Feng, M. R. Wasielewski, S. I. Stupp and J. F. Stoddart, *J. Am. Chem. Soc.*, 2021, **143**, 8000–8010.

19 S. Dey, B. Mondal, S. Chatterjee, A. Rana, S. Amanullah and A. Dey, *Nat. Rev. Chem.*, 2017, **1**, 0098.

20 M. Haake, D. Aldakov, P. Julien, G. Veronesi, A. A. Tapia, B. Reuillard and V. Artero, *J. Am. Chem. Soc.*, 2024, **146**, 15345–15355.

21 S. Sung, D. Kumar, M. Gil-Sepulcre and M. Nippe, *J. Am. Chem. Soc.*, 2017, **139**, 13993–13996.

22 Y. Cheng, J. Peng, G. Lai, X. Yue, F. Li, Q. Wang, L. Chen and J. Gu, *ACS Catal.*, 2024, **14**, 8446–8455.

23 M. Tamtaji, M. G. Kim, J. Wang, P. R. Galligan, H. Zhu, F. Hung, Z. Xu, Y. Zhu, Z. Luo, W. A. G. Iii and G. Chen, *Adv. Sci.*, 2024, **11**, 2309883.

24 Q. Zhang, C. B. Musgrave, Y. Song, J. Su, L. Huang, L. Cheng, G. Li, Y. Liu, Y. Xin, Q. Hu, G. Ye, H. Shen, X. Wang, B. Z. Tang, W. A. Goddard and R. Ye, *Nat. Synth.*, 2024, **3**, 1231–1242.

25 N. Sakamoto, K. Sekizawa, S. Shirai, T. Nonaka, T. Arai, S. Sato and T. Morikawa, *Nat. Catal.*, 2024, **7**, 574–584.

26 A. Tamtögl, M. Sacchi, V. Schwab, M. M. Koza and P. Fouquet, *Commun. Chem.*, 2024, **7**, 78.

27 T. Liu, H. Qin, Y. Xu, X. Peng, W. Zhang and R. Cao, *ACS Catal.*, 2024, **14**, 6644–6649.

28 M. Tamtaji, S. Kwon, C. B. Musgrave, W. A. Goddard and G. Chen, *ACS Appl. Mater. Interfaces*, 2024, **16**, 50567–50575.

29 M. Tamtaji, M. G. Kim, Z. Li, S. Cai, W. Jun, P. R. Galligan, F.-F. Hung, H. Guo, S. Chen, W. A. G. III and Z. Luo, *Nano Energy*, 2024, **126**, 109634.

30 J. Feng, L. Wu, S. Liu, L. Xu, X. Song, L. Zhang, Q. Zhu, X. Kang, X. Sun and B. Han, *J. Am. Chem. Soc.*, 2023, **145**, 9857–9866.

31 W. Xia, Y. Xie, S. Jia, S. Han, R. Qi, T. Chen, X. Xing, T. Yao, D. Zhou, X. Dong, J. Zhai, J. Li, J. He, D. Jiang, Y. Yamauchi, M. He, H. Wu and B. Han, *J. Am. Chem. Soc.*, 2023, **145**, 17253–17264.

32 J. Chen, T. Wang, X. Wang, B. Yang, X. Sang, S. Zheng, S. Yao, Z. Li, Q. Zhang, L. Lei, J. Xu, L. Dai and Y. Hou, *Adv. Funct. Mater.*, 2022, **32**, 2110174.

33 J. Leverett, T. Tran-Phu, J. A. Yuwono, P. Kumar, C. Kim, Q. Zhai, C. Han, J. Qu, J. Cairney, A. N. Simonov, R. K. Hocking, L. Dai, R. Daiyan and R. Amal, *Adv. Energy Mater.*, 2022, **12**, 2201500.

34 C. Du, J. P. Mills, A. G. Yohannes, W. Wei, L. Wang, S. Lu, J. Lian, M. Wang, T. Guo, X. Wang, H. Zhou, C. Sun, J. Z. Wen, B. Kendall, M. Couillard, H. Guo, Z. Tan, S. Siahrostami and Y. A. Wu, *Nat. Commun.*, 2023, **14**, 6142.

35 I. Jang, S. Lee, D. Kim, V. K. Paidi, S. Lee, N. Dong, J. Y. Jung, K. Lee, H. Lim, P. Kim and S. Jong, *Adv. Mater.*, 2024, **36**, 2403273.

36 Z. Bai, X. Z. Jiang and K. H. Luo, *Phys. Chem. Chem. Phys.*, 2023, **25**, 23717–23727.

37 Q. Zhao, M. Zhang, Y. Gao, H. Dong, L. Zheng, Y. Zhang, J. Ouyang and N. Na, *J. Am. Chem. Soc.*, 2024, **146**, 14875–14888.

38 Z. Qiao, R. Jiang, H. Xu, D. Cao and X. C. Zeng, *Angew. Chemie Int. Ed.*, 2024, **136**, e202407812.

39 X. Rong, H. J. Wang, X. L. Lu, R. Si and T. B. Lu, *Angew. Chemie - Int. Ed.*, 2020, **59**, 1961–1965.

40 X. Wang, Q. Zhang and J. Zhou, *J. Colloid Interface Sci.*, 2022, **610**, 546–556.

41 M. K. Wong, J. J. Foo, J. Y. Loh and W. J. Ong, *Adv. Energy Mater.*, 2024, **14**, 2303281.

42 M. Tamtaji, Y. Li, Y. C. Cai, H. Liu, W. A. G. III and G. Chen, *J. Mater. Chem. A*, 2023, **11**, 25410–25421.

43 M. Tamtaji, W. A. Goddard III, Z. Hu and G. H. Chen, *J. Mater. Sci. Technol.*, 2025, **218**, 126–134.

44 X. Liu, Z. Zhang, Z. Xing, L. Xianglin and C. Cheng1, *Res. Sq.*, 2024, 1–25.

45 C. B. Musgrave, Y. Li, Z. Luo and W. A. Goddard, *Nano Energy*, 2023, **118**, 108966.

46 J. Gao, A. Bahmanpour, O. Kröcher, S. M. Zakeeruddin, D. Ren and M. Grätzel, *Nat. Chem.*, 2023, **15**, 705–713.

47 S. Grimme, S. Ehrlich and L. Goerigk, *J. Comput. Chem.*, 2011, **32**, 1456–1465.

48 N. M. Twyman, A. Walsh and T. Buonassisi, *Chem. Mater.*, 2022, **34**, 2545–2552.

49 C. J. Bartel, A. Trewartha, Q. Wang, A. Dunn, A. Jain and G. Ceder, *npj Comput. Mater.*, 2020, **6**, 97.

50 Z. Xue, R. Tan, J. Tian, H. Hou, X. Zhang and Y. Zhao, *J. Colloid Interface Sci.*, 2024, **674**, 353–360.

51 C. Wang, *Commun. Chem.*, 2024, **7**, 9.

52 J. M. Gallagher, B. M. W. Roberts, S. Borsley and D. A. Leigh, *Chem*, 2024, **10**, 855–866.

53 M. Tamtaji, M. Kazemeini and J. Abdi, *Int. J. Hydrogen Energy*, 2024, **80**, 1075–1083.

54 M. Tamtaji, Q. Peng, T. Liu, X. Zhao, Z. Xu, P. R. Galligan, M. D. Hossain, Z. Liu, H. Wong, H. Liu, K. Amine, Y. Zhu, W. A. Goddard, W. Wu and Z. Luo, *Nano Energy*, 2023, **108**, 108218.

55 M. D. Hossain, Z. Liu, M. Zhuang, X. Yan, G. L. Xu, C. A. Gadre, A. Tyagi, I. H. Abidi,

C. J. Sun, H. Wong, A. Guda, Y. Hao, X. Pan, K. Amine and Z. Luo, *Adv. Energy Mater.*, 2019, **9**, 1803689.

56 Y. Huang, F. Rehman, M. Tamtaji, X. Li, Y. Huang, T. Zhang and Z. Luo, *J. Mater. Chem. A*, 2021, **10**, 5813–5834.

57 L. Yu, F. Li, J. Huang, B. G. Sumpter, W. E. Mustain and Z. Chen, *ACS Catal.*, 2023, **13**, 9616–9628.

58 Q. Zhou, X. Tang, S. Qiu, L. Wang, L. Hao and Y. Yu, *Mater. Today Phys.*, 2023, **33**, 101050.

59 J. Xiao, J. J. Masana, H. Dong, H. Zhang, H. Yang, M. Qiu and Y. Yu, *J. Mater. Chem. A*, 2023, **11**, 24359–24370.

60 H. Xu, D. Cheng, D. Cao and X. C. Zeng, *Nat. Catal.*, 2018, **1**, 339–348.

61 J. Zhang, A. Yu and C. Sun, *Appl. Surf. Sci.*, 2022, **605**, 154534.

62 L. Yu, F. Li, J. Zhao and Z. Chen, *Adv. Powder Mater.*, 2022, **1**, 100031.

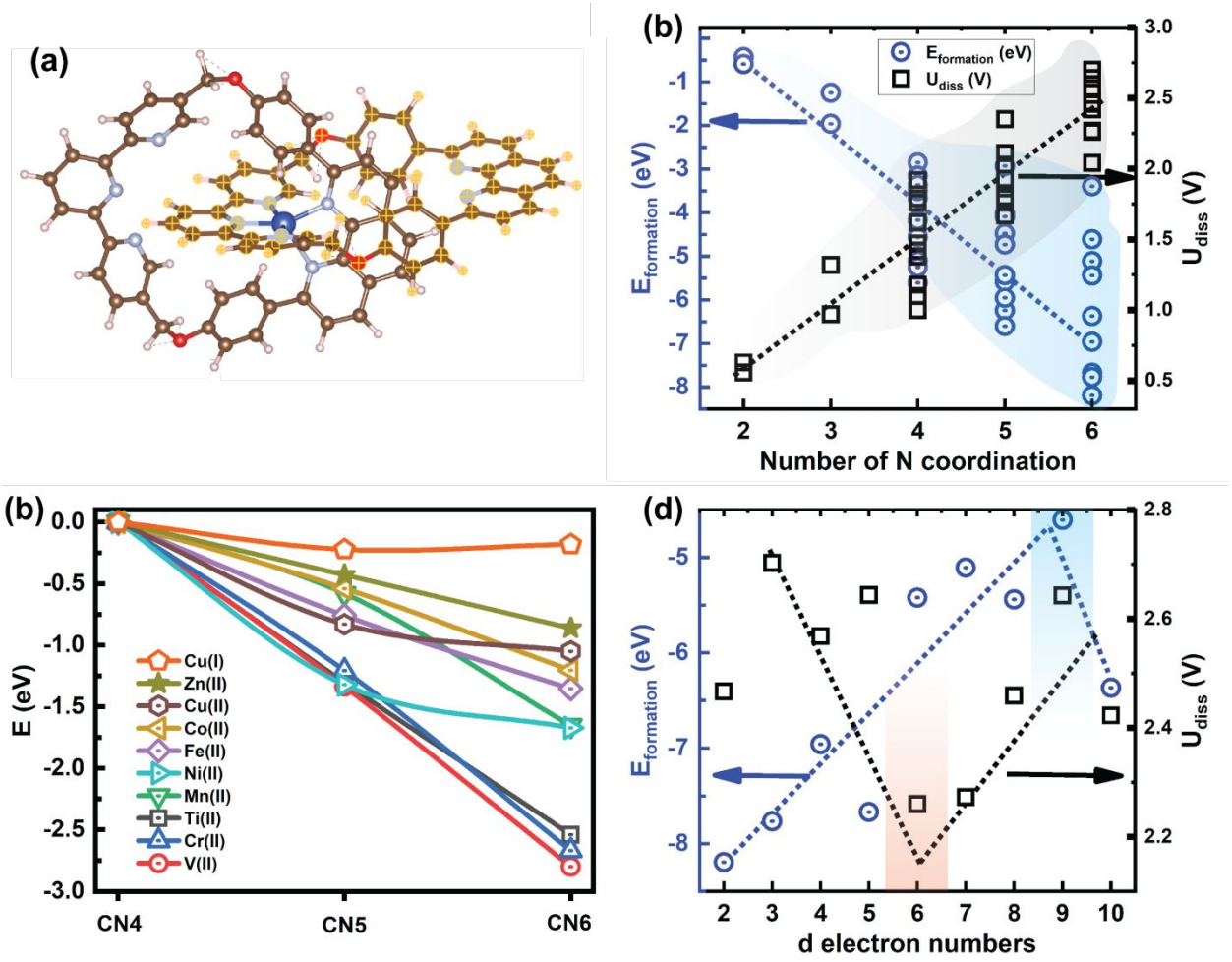

Figure 1. Mechanically interlocked metal complex. (a) The structure of M(I or II)$_{CNx=4,5,6}$ which M represents 3d transition metals. Brown, light blue, and dark blue balls show C, N, and M elements, respectively. (b) Dissolution potential and formation energy for M(I or II)$_{CNx=2,3,4,5,6}$ versus the number of nitrogen atoms around the metal, indicating all the candidates meet the electrochemical and thermodynamic stability criteria (U_{diss}>0 and $E_{formation}$<0). (c) The change in the energy of M(I or II)$_{CNx=4,5,6}$ with different nitrogen atoms. (d) Volcano plot for the formation energy and dissolution potential against the number of d orbital electrons for M(II)$_{CN6}$ suggesting the minimum formation energy at the d electron number of 9 and lowest dissolution potential at the d electron number of 6.

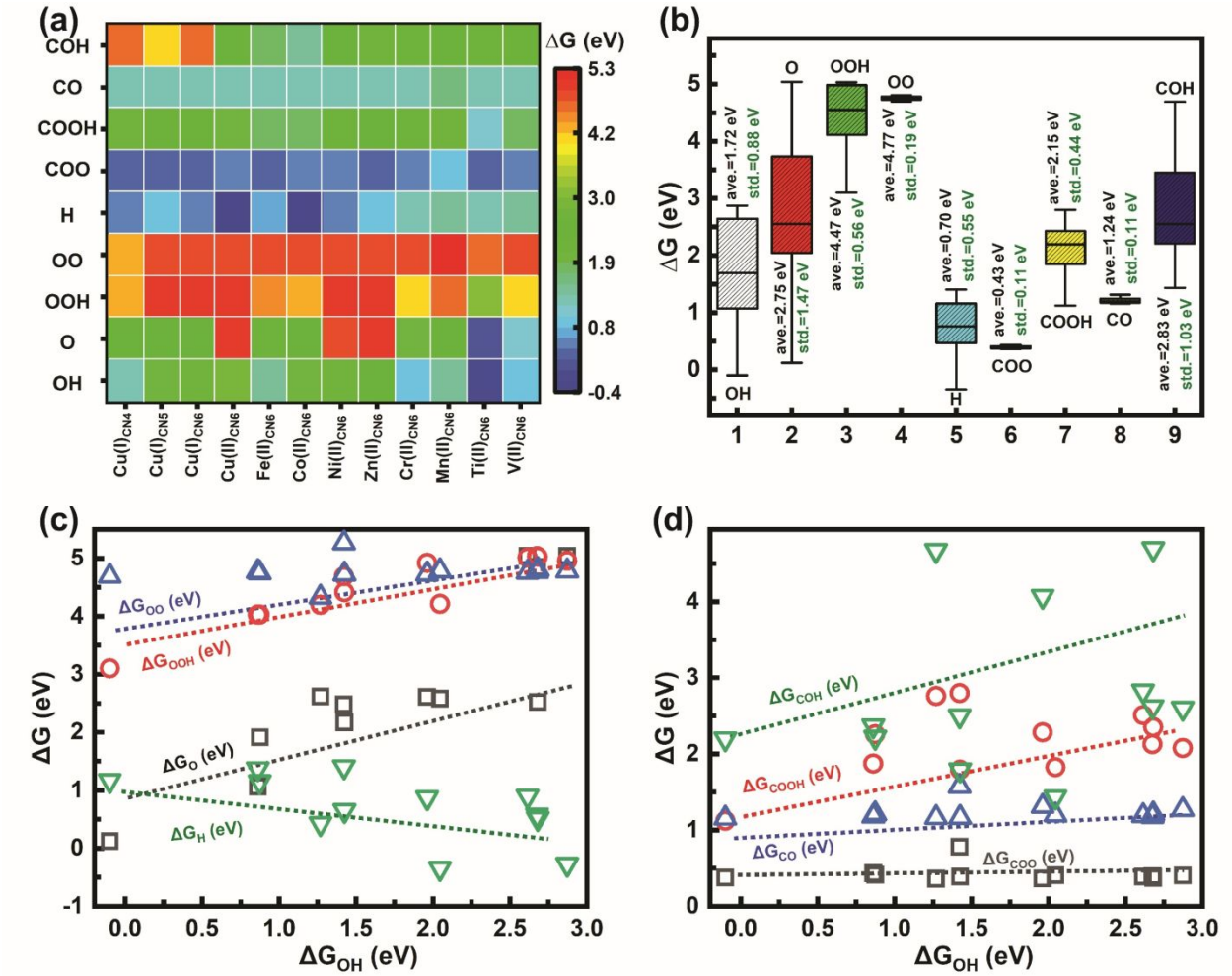

Figure 2. Gibbs free energy analysis. (a) DFT-obtained Gibbs free energy of reaction intermediates for $M(II)_{CN6}$. (b) Box plot of Gibbs free energy variation of each reaction intermediates. (c,d) Analysis of the weakened scaling relationship limits among the intermediates.

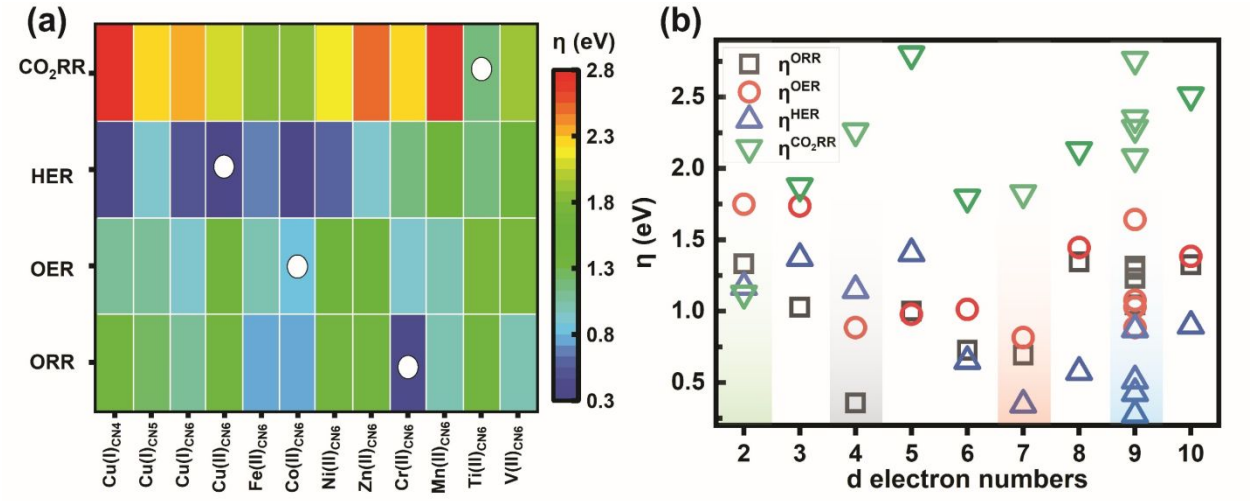

Figure 3. Overpotentials. (a) High throughput screening of DFT-calculated CO_2RR, HER, OER, and ORR overpotentials. (b) Volcano plot of DFT-obtained CO_2RR, HER, OER, and ORR overpotentials against the number of d orbital electrons suggesting the lowest overpotentials at d electron number of 7.

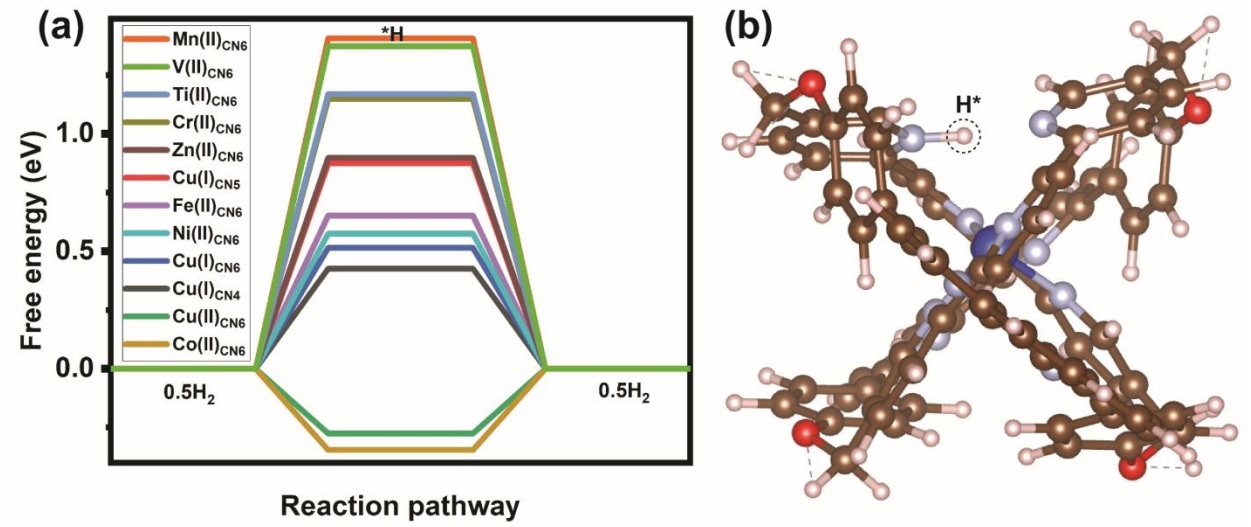

Figure 4. HER. (a) HER pathways for metal complexes, indicating $Cu(II)_{CN6}$ with HER overpotentials 0.27 V_{RHE}. (b) The side view of H intermediate on nitrogen active site of $Cu(II)_{CN6}$.

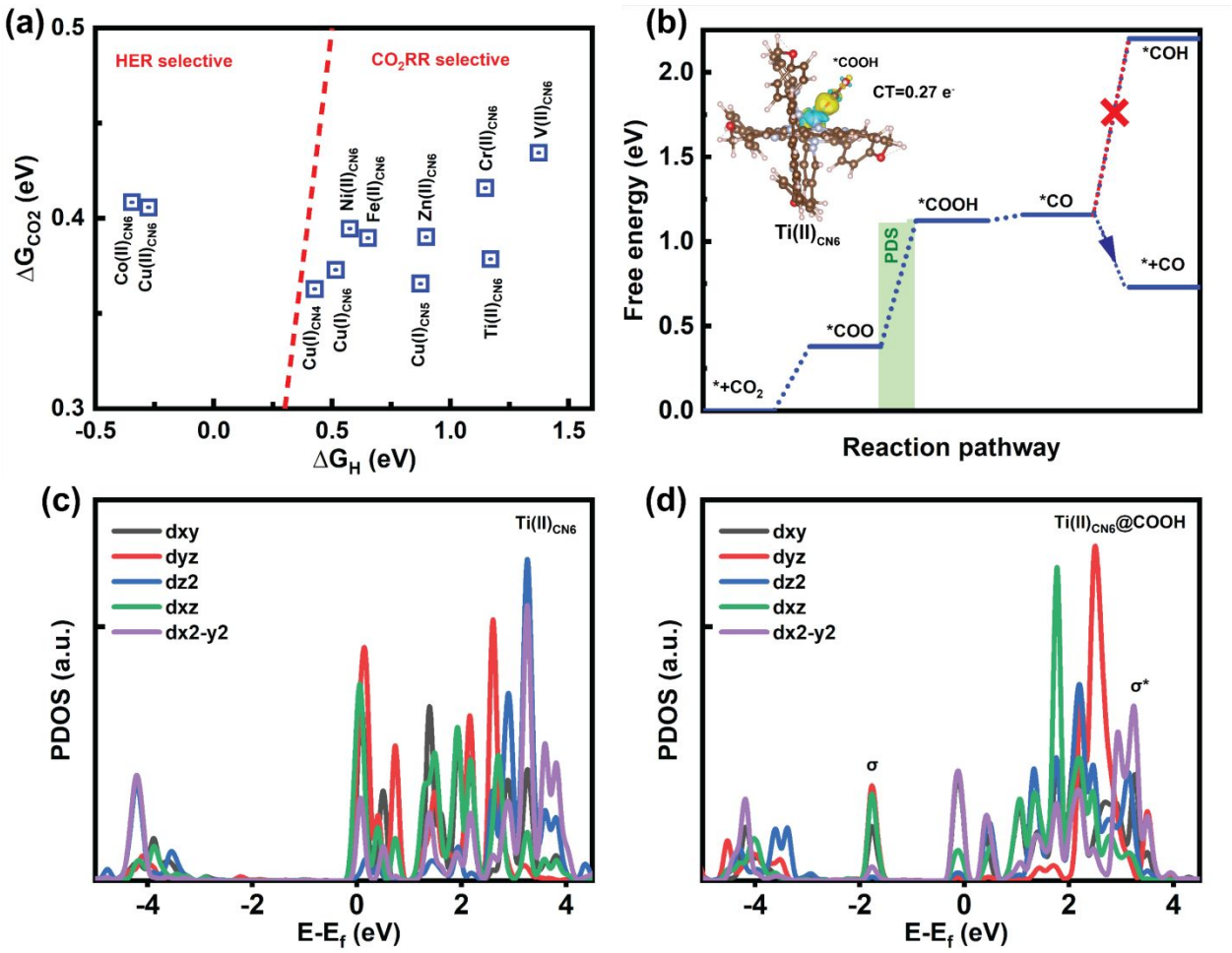

Figure 5. CO_2RR pathway. (a) ΔG of CO_2 versus ΔG of H for $M(II)_{CN6}$ and $Cu(I)_{CNx=4,5,6}$, showing that all the structures except for $Co(II)_{CN6}$ and $Cu(II)_{CN6}$ are CO_2RR selective on the surface. (b) CO_2RR pathway for $Ti(II)_{CN6}$ with CO_2RR overpotential of 1.12 V_{RHE}. The inset displays the side view of the Bader charge transfer from $Ti(II)_{CN6}$ to COOH with the Isosurface value of 0.005 e/Å^3. Blue color shows the region of charge deficiency and yellow color shows the region of charge availability. Partial density of states (PDOS) of $3d_{x2-y2}$, $3d_{z2}$, $3d_{xz}$, $3d_{xy}$, and $3d_{yz}$ orbitals of Ti active site in $Ti(II)_{CN6}$ (c) in the absence and (d) in the presence of COOH intermediate.

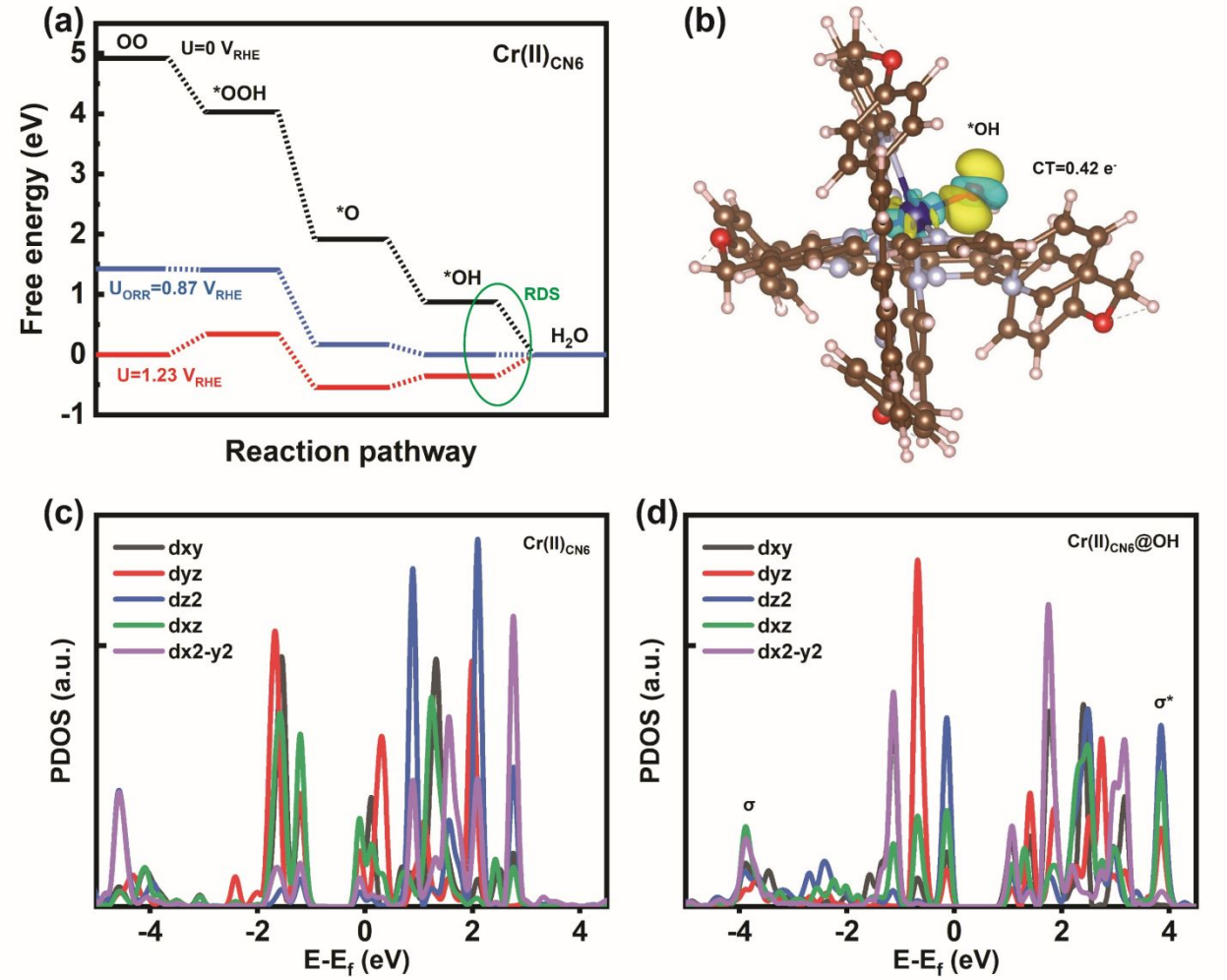

Figure 6. ORR pathway. (a) ORR pathway for $Cr(II)_{CN6}$ with ORR overpotential of 1.15 V_{RHE}. (b) The side view of the Bader charge transfer from $Cr(II)_{CN6}$ to OH with the Isosurface value of 0.005 e/Å^3. Blue color shows the region of charge deficiency and yellow color shows the region of charge availability. Partial density of states (PDOS) of $3d_{x2-y2}$, $3d_{z2}$, $3d_{xz}$, $3d_{xy}$, and $3d_{yz}$ orbitals of Cr atom in $Cr(II)_{CN6}$ (c) in the absence and (d) in the presence of OH intermediate.

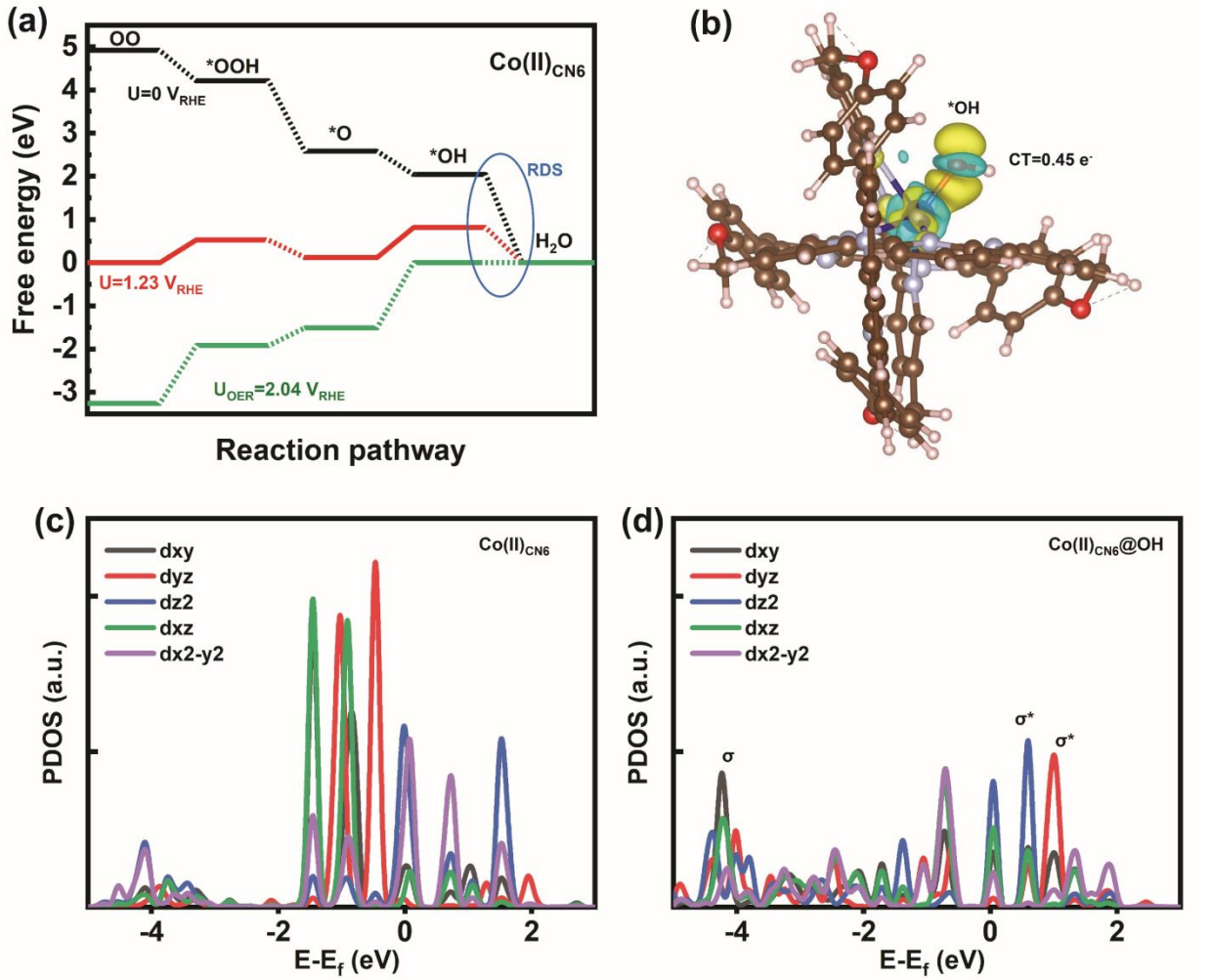

Figure 7. OER pathway. (a) OER pathway for $Co(II)_{CN6}$ with OER overpotential of 0.79 V_{RHE}. (b) The side view of the Bader charge transfer from $Co(II)_{CN6}$ to OH with the Isosurface value of 0.005 e/Å^3. Blue color shows the region of charge deficiency and yellow color shows the region of charge availability. Partial density of states (PDOS) of $3d_{x2-y2}$, $3d_{z2}$, $3d_{xz}$, $3d_{xy}$, and $3d_{yz}$ orbitals of Cr atom in $Co(II)_{CN6}$ (c) in the absence and (d) in the presence of OH intermediate.

Data availability

Data will be available on request.